Electrical transport and pinning properties of Nb thin films patterned with focused ion beam-milled washboard nanostructures

2012 New J. Phys. 14 113027

(http://iopscience.iop.org/1367-2630/14/11/113027)

New Journal of Physics
The open access journal for physics

Electrical transport and pinning properties of Nb thin films patterned with focused ion beam-milled washboard nanostructures

O V Dobrovolskiy[1,4], E Begun[1], M Huth[1] and V A Shklovskij[2,3]

[1] Physikalisches Institut, Goethe-University, 60438 Frankfurt am Main, Germany

[2] Institute of Theoretical Physics, NSC-KIPT, 61108 Kharkiv, Ukraine

[3] Physical Department, Kharkiv National University, 61077 Kharkiv, Ukraine

E-mail: Dobrovolskiy@Physik.uni-frankfurt.de

New Journal of Physics **14** (2012) 113027 (27pp)

Received 17 July 2012

Published 22 November 2012

Online at http://www.njp.org/

doi:10.1088/1367-2630/14/11/113027

Abstract. A careful analysis of the magneto-transport properties of epitaxial nanostructured Nb thin films in the normal and the mixed state is performed. The nanopatterns were prepared by focused ion beam (FIB) milling. They provide a washboard-like pinning potential landscape for vortices in the mixed state and simultaneously cause a resistivity anisotropy in the normal state. Two matching magnetic fields for the vortex lattice with the underlying nanostructures have been observed. By applying these fields, the most likely pinning sites along which the flux lines move through the samples have been selected. By this, either the background isotropic pinning of the pristine film or the enhanced isotropic pinning originating from the nanoprocessing have been probed. Via an Arrhenius analysis of the resistivity data the pinning activation energies for three vortex lattice parameters have been quantified. The changes in the electrical transport and the pinning properties have been correlated with the results of the microstructural and topographical characterization of the FIB-patterned samples. Accordingly, along with the surface processing, FIB milling has been found to alter the material composition and the degree of disorder in as-grown films. The obtained results provide further insight into the pinning mechanisms at work in FIB-nanopatterned superconductors, e.g. for fluxonic applications.

[4] Author to whom any correspondence should be addressed.

Contents

1. Introduction

Within the last decade, nanostructured superconductors have received much attention [1–3]. They provide direct access to the manipulation of fluxons, i.e. Abrikosov vortices, with the help of tailored pinning potentials. This is due to the fact that Abrikosov vortices, which are very sensitive to the alterations of the superconducting order parameter [4, 5], represent a very useful tool for probing pinning and, thus, the degree of structural disorder associated with it in different parts of a nanostructured superconductor. To control vortex motion by suitable defects and their arrangement, an array of pinning sites is usually used [1–3]. An accurate adjustment of the fluxons dynamics is achieved by fine-tuning the magnetic field. Accordingly, the study of the pinning and flux-flow properties [6–8], the dynamic phases and the ordering [9–12], the flux-flow instability [13–15] and the vortex lattice commensurability [16–19], the vortex guiding [2, 20–22] and the ratchet [2, 3, 23–25] effect in type II superconductors is of great interest with regard to both basic research and the development of fluxonic applications.

Various techniques have been used to provide different pinning sites in the form of dots [26, 27], (blind) antidots [22–25], stripes [28] and more complex nonmagnetic [16–19] and magnetic [29–31] (nano)structures. All these approaches share the problem that a full and exact

theoretical description of the two-dimensional nonlinear vortex dynamics in these systems has not been available so far. On the other hand, very few experiments have been performed on thin films for a simpler model case in which the nano-engineered pinning potential is assumed to be periodic in one direction, i.e. is of the washboard type. For a washboard pinning potential (WPP) the magneto-resistive response of the sample can be accounted for [32–34] exactly, at least in the single-vortex approximation. Therefore, washboard-like nanostructures arguably represent the most suitable model system for studying the temperature-dependent nonlinear single-vortex dynamics at arbitrary values of temperature, current density and angle between the direction of the transport current and the WPP guiding channels.

A successful approach for the experimental realization of a washboard-like pinning potential has been used by Soroka *et al* [20], who employed self-organized semi-periodic, linearly extended pinning 'sites' in thin Nb films grown by molecular beam epitaxy on facetted sapphire substrate surfaces [35]. There it has been demonstrated [20] that a pronounced guiding of vortices occurs. Another approach, which is based on the direct nanopatterning by focused particle beam techniques [36], has been used to provide washboard-like pinning nanostructures in the form of milled grooves [37] or Co stripes [38, 39] on the top of Nb films. Our preliminary results [37–40] have shown that anisotropic (a) pinning effects are even more clearly seen in these highly periodic structures. In particular, Nb films, decorated by an array of ferromagnetic Co stripes [38, 39] by means of focused electron beam-induced deposition, demonstrate a pronounced anisotropy of the magneto-resistivity. However, for a quantitative comparison of that experiment [38, 39] with the theory [32–34], an additional complexity arises due to the different possible magnetization states in the Co stripes. In this work, in order to fabricate a WPP without such complexity, we decided to use a complementary technique, focused ion beam (FIB) milling, in order to fabricate a set of nanostructures tilted at different angles with respect to the transport current direction. These nanostructures represent a very accurate realization of the WPP on the basis of which the theoretical predictions of [32–34] can be examined. To our knowledge, so far there have been very few works [6] utilizing FIB-patterned, washboard-like pinning structures. A detailed study of the interrelated changes in the structural, magneto-transport and pinning properties of FIB-patterned films has not been performed until now.

Firstly, a complete characterization of the resistive properties of FIB-patterned superconducting samples in both the normal and the mixed state has not been accomplished so far. Secondly, an important aspect is properly accounting for changes in the magneto-resistive response of as-grown films and how these are modified by nanoprocessing in patterned samples. In particular, it was previously found that FIB patterning with Ga ions at an energy of 30 kV has no influence on the pinning properties of 300 nm-thick Nb [6] and 250 nm-thick YBCO [24] films. For thinner films and for a wider range of irradiation doses this has not been studied in detail. Thirdly, from geometrical considerations of the cross-section geometry, the normal-state resistive response must also depend on the angle at which the nanostructure is tilted with respect to the transport current direction. Then, this normal-state resistivity anisotropy must be accounted for when more subtle phenomena, such as the pinning anisotropy in the mixed state [41], have to be analyzed. Finally, it is necessary to correlate the pinning activation energy with the changes in the material composition and the degree of structural disorder that arise due to nanostructuring. In the theory [32–34], the pinning strength is characterized by the depth of the pinning potential, its width and its period. An estimation of these values for

FIB-nanostructured samples is necessary for a reliable quantitative comparison of magnetoresistivity data [41] with the theory [32–34]. Besides, these estimates can be used for pinning potentials of other types [42, 43]. This paper aims to clarify all these questions.

The paper is organized as follows. The sample preparation and the microstructural and topographical characterization of the samples are reported in section 2. The electrical transport properties of the samples in the normal state are discussed in section 3. An account of the mixed-state properties of the patterned films is given in section 4. The central results of the paper are compiled in section 5, where the pinning potentials are quantified with the help of an Arrhenius' analysis of the even longitudinal resistivity component, and the pinning enhancement mechanisms in the FIB-patterned samples are elucidated. In section 6, we summarize our results.

2. Sample preparation and characterization

2.1. Sample preparation

By means of a single deposition process, two nominally identical epitaxial Nb (110) films with a thickness of 52 nm were prepared by dc magnetron sputtering onto $(11\bar{2}0)$ sapphire substrates cut from one and the same α-Al_2O_3 wafer. During the deposition process the substrates were kept at $T_s = 850\,^{\circ}\mathrm{C}$, the Ar pressure was $p_s = 4 \times 10^{-3}$ mbar and the growth rate was $g \simeq 1\,\mathrm{nm\,s^{-1}}$. For further details of the samples preparation and their structural characterization, see [44]. Both films were pre-patterned by standard photolithography followed by Ar ion-beam etching in order to define eight 4-contact structures with an intersection area of $30 \times 100\,\mu\mathrm{m}^2$. One sample has been left unpatterned for reference purposes and seven others have been nanostructured. Below, each patterned structure will be referred to by the angle value by which it is tilted with respect to the long strip of the bridge.

2.2. Nanopattern fabrication

Nanopatterning was performed by FIB in a high-resolution SEM (FEI Nova NanoLab 600). For the patterning process, the beam parameters were 30 kV/30 pA in normal incidence and the dwell time was 1 μs. The sample was tilted by 52° with respect to the electron beam column. To predetermine the average groove depth h, *in situ* measurements of the electrical resistivity (see [45]), as a function of the number of ion beam passes, have been made for two bridges fabricated in an additional Nb film with the same thickness d of 52 nm. The data thus collected are shown in figure 1. These are accompanied by fits on the basis of a simple model described in section 3.3. As is evident from the figure, the milling of grooves across the long strip of the bridge ($\alpha = 90^{\circ}$) leads to infinite resistance of the structure when $h/d = 1$, i.e. the bridge is completely cut off, as is expected. The complete cutoff of the 52 nm-thick bridge occurs at 32 000 ion beam passes. We pre-determined h as 8 nm by stopping the milling at 5000 beam passes. This value was used for patterning all the bridge structures. We considered it to be sufficient to provide strong a pins and, at the same time, to keep the difference in resistance of the bridges patterned with different α values small. From figure 1, it follows that the resistance of the bridge for $\alpha = 0^{\circ}$ is much less changed by milling than that for $\alpha = 90^{\circ}$, as expected from the geometry. It is worth noting that with an increase of the groove depth h the difference in film resistances $\delta\rho \equiv [\rho(0^{\circ}) - \rho(90^{\circ})]/\rho(0^{\circ})$ becomes more pronounced. Here $\delta\rho$ characterizes the normal-state resistivity anisotropy.

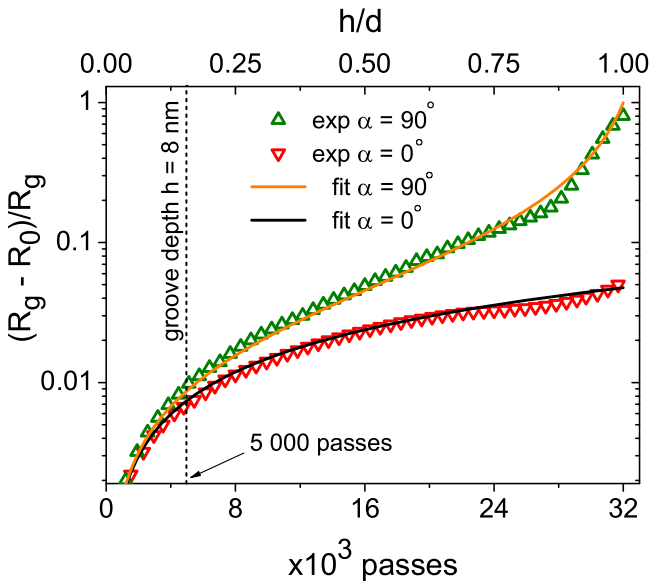

Figure 1. *In situ* recorded changes in the electrical resistance R_g of two 52 nm-thick Nb film structures during FIB patterning. The relative change of the resistance compared to the resistance of the unpatterned structure is shown as a function of the ion beam pass number. The nanostructure is an array of periodically arranged and uniaxially oriented grooves milled along ($\triangledown$, $\alpha = 0°$) and across ($\triangle$, $\alpha = 90°$) the long strip of the bridge, as shown in figure 2. The solid lines are fits by equations (3) and (4), see text for details. The upper axis shows the ratio of the groove depth h to the film thickness d.

Whereas the pre-defined nanoprofile (see figure 2) was one and the same for all the structures, each bridge was patterned with one of the following values of α: 0°, 15°, 30°, 45°, 60°, 75° and 90°. In order to avoid marginal effects, the nanopatterning area was set to $160 \times 32\,\mu\text{m}^2$, i.e. as slightly larger than the bridge dimensions. The alignment of the nanopattern is shown in figure 2(a). The thus obtained samples allowed us to measure the longitudinal ($\parallel$) and transverse ($\perp$) voltages for different α values.

2.3. Material composition

The gallium ion beam is known to cause amorphization, implantation and vacancy generation in the near-surface area of the processed region [36]. In particular, calculations using Monte Carlo simulations [46] indicate that an implantation of Ga ions occurs chiefly at a depth of up to approximately 12 nm of the Nb film in the present case[5]. We performed an inspection using energy-dispersive x-ray spectroscopy (EDX) in the SEM right after the nanostructuring, without exposure of the samples to air. Specifically, four tests have been made: probed were one patterned film and one as-grown film, with a test area of $1 \times 1\,\mu\text{m}^2$, as well as one region between two neighboring grooves and one region containing a groove, with a test area of $100 \times 100\,\text{nm}^2$. The EDX parameters were 5 kV and 1.6 nA. Here the beam energy

[5] The stopping of the Ga ions in the Nb film was simulated with the help of SRIM software available under http://www.srim.org/.

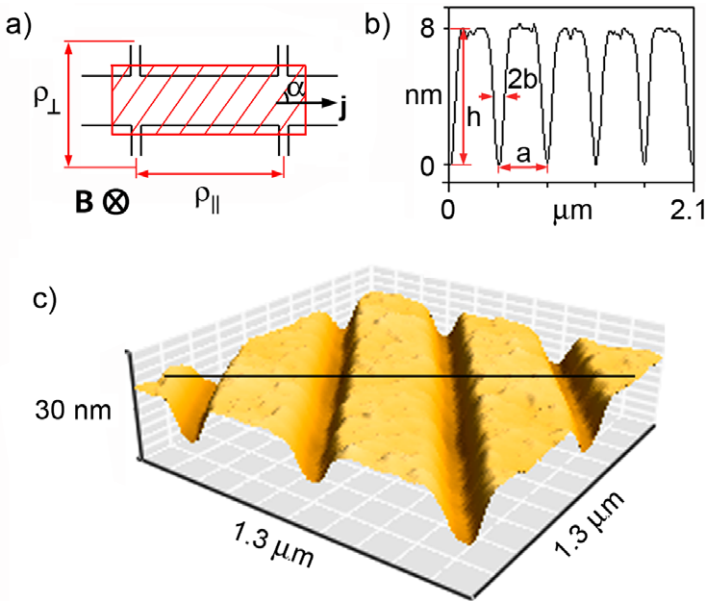

Figure 2. (a) Sample configuration in the general case: the Nb film with a thickness of 52 nm is placed in a small perpendicular magnetic field $B \ll B_{c2}(T)$ at a temperature close to T_c. A small transport current density **j** is applied to the sample. Experimentally deducible values are the longitudinal $\rho_{\parallel}$ and the transverse $\rho_{\perp}$ magneto-resistivities, determined relative to the direction of **j**. Seven bridges were nanostructured with the pinning profile tilted at an angle α of 0°, 15°, 30°, 45°, 60°, 75° and 90° with regard to the **j**-direction. One bridge was left non-structured for reference purpose. Quantitatively, T_c is 8.61 K, the j used is 0.7 or 6.4 kA cm^{-2}, and a field B of 8.8 mT corresponds to the fundamental matching field of the vortex ensemble with the underlying 420 nm-periodic washboard-like profile. (b) Cross-section scan with the pinning nanoprofile parameters deduced along the black line in the AFM image of the sample surface taken in non-contact mode (c). The symbols $a = 420 \pm 2$ nm, $h = 8 \pm 0.5$ nm and $2b = 60 \pm 3$ nm denote the average pinning potential period, depth and the full-width at half-depth of a groove, respectively.

determines the effective thickness of the layer being analyzed, which is approximately 45 nm.[6] This corresponds to approximately 90% of the electron beam energy dissipated in the film. The material composition was calculated taking into account ZAF (atomic number, absorbtion and fluorescence) and background corrections. The software we used to analyze the material composition in the film was EDAX's Genesis Spectrum v. 5.11. The statistical error in the elemental composition is 1.5%.

The raw data (not shown) demonstrate peaks of four elemental materials: Nb, O, Al and Ga. The peaks corresponding to O and Al arise due to the relatively thin film thickness such that the contribution from the substrate (Al_2O_3) cannot be avoided. A small fraction of the O peak area arises from the top 2 nm oxide layer of the Nb film [47]. This oxidized layer is formed

[6] The penetration of the electrons into the film was calculated by the simulation program Casino available at http://www.gel.usherbrooke.ca/casino/index.html.

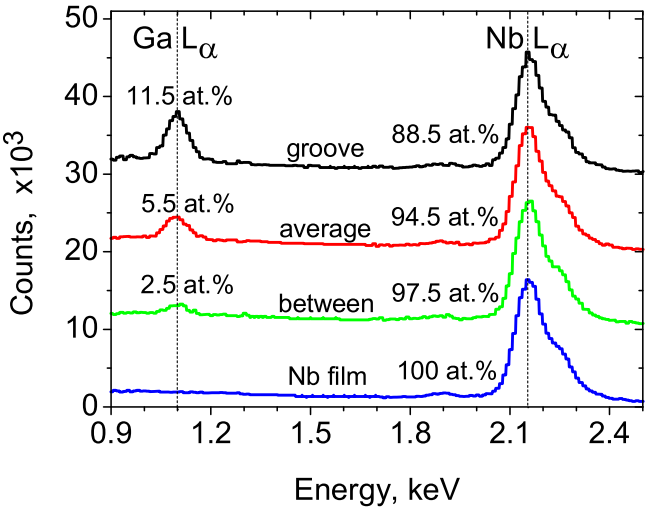

Figure 3. Material composition in the as-grown film and the same film after the nanostructuring (probed area of $1 \times 1\,\mu m^2$), as well as between grooves and in the groove area (probed area of $100 \times 100\,nm^2$) revealed by energy-dispersive x-ray spectroscopy. Along the vertical axis, an offset of 10^3 counts is used to facilitate comparison. The data were normalized in such a way that the sum of the content of Ga and Nb in the sample is 100 at.%. The peaks of Ga and Nb are shown by vertical dashed lines.

during the first seconds after the film had been taken out from the sputtering system. It serves as a protection layer preventing further oxidation of the film. The peaks of Al and O do not vary from test to test so that all spectra in figure 3 are normalized in such a way that the sum of the content of Ga and Nb in the sample is 100 at.%. We now compare these EDX spectra in detail.

Firstly, the test made on the as-grown Nb film shows 100 at.% of Nb, which is our reference. All the FIB-patterned structures show Ga apart from the dominating Nb peak. We note that the test area taken over $1\,\mu m^2$ in the patterned sample includes two grooves and the area close by. Thus, the content of 5.5 at.% can be considered as the *average* content of Ga in the nanostructure. This is a strong indication that the material composition in the patterned structures is changed with respect to that of the as-grown film. To answer the question of whether there is any variation in the content of Ga in different regions of the pattern, the in-groove area and the area between the grooves have been probed. According to figure 3, the in-groove spectrum reveals 11.5 at.% of Ga. At the same time, 2.5 at.% of Ga is found in the patterned structure away from the grooves. This must be due to secondary and high-order collisions of Ga ions with Nb atoms.

2.4. Topographical characterization

A post-patterning SEM inspection of various linearly extended pinning nanostructures, chiefly to check the highest achievable resolution of FIB, has been reported in a previous paper [40]. In this paper, we present the results of a more careful analysis of the fabricated nanopatterns by atomic force microscopy (AFM). For high-resolution morphology characterization, AFM under ambient conditions in non-contact, dynamic force mode was used. The cantilever tip was shaped

like a polygon-based pyramid, with a tip radius of less than 7 nm (Nanosensors PPP-NCLR), so that convolution effects due to the finite tip radius can be neglected. An exemplary AFM image of the fabricated structure is shown in figures 2(b) and (c). The pattern is a system of uniaxially directed and periodically arranged grooves (trenches) with a period a of 420 ± 2 nm. The overall shape of the nanofabricated structure is visually identical over the whole area of a bridge and does not vary from bridge to bridge. The angle α is found to deviate from its pre-defined values by less than 0.3°. This error originates from an unavoidable rotatory misalignment of the sample stage with respect to the bitmap pattern in the SEM. The peak-to-peak surface roughness Δd of the as-grown film is about 1.5 nm. Between grooves, all the patterned samples show an increased Δd of 2.5–3 nm. We attribute this increase to the presence of a small amount of Nb and, probably, a minor amount of Ga settled onto the film surface during the nanostructuring. Niobium must have been milled out from the groove regions, whereas Ga may originate from the focused ions first implanted into the film and subsequently knocked out by the FIB again.

From a line scan across the grooves (see figure 2(b)) we deduce a groove width at half-depth $2b$ of 60 ± 3 nm and a groove depth h of 8 ± 0.5 nm. We note that the smallest test area achievable with our EDX technique is larger than $2b$ of a groove. Hence, the value of Ga at the groove bottom revealed by EDX in the previous subsection seems to be slightly underestimated. Consequently, it is safe to believe that the content of Ga at the groove bottom is around 15 at.% as the most probable implantation of Ga is expected underneath the bottom of the grooves. From the lateral groove parameters we estimate the relative volume fraction $\varepsilon = 2b/a$ occupied by a groove as 1/7. From a line scan along the groove bottom (not shown) a peak-to-peak roughness of approximately 1 nm is measured. All these circumstances allow us to conclude that the motion of vortices in such a fabricated structure can be theoretically described as their motion in some periodic pinning potential of the washboard type. So the nanostructure shown in figure 2 represents a reasonable experimental realization of the anisotropic WPP used for theoretical modeling in [32–34].

All the samples were wire bonded and mounted onto the sample holder of a ^{4}He cryostat with a superconducting solenoid. All the magneto-resistivity measurements were made in external fields $+\mathbf{B}$ and $-\mathbf{B}$ directed perpendicular to the film surface. The even and odd magneto-resistivity components were calculated according to the relation

$$\rho^{\pm} = [\rho(+\mathbf{B}) \pm \rho(-\mathbf{B})]/2. \tag{1}$$

The normal-state and superconducting properties of the samples are reported next.

3. Normal-state properties

3.1. Zero-field cooling

Typical zero-field cooling (ZFC) curves for the non-structured (as-grown) and one patterned sample with $\alpha = 0^\circ$ are shown in figure 4. The curves $\rho(T)$ were measured with the four-point dc resistive method. Both curves demonstrate an almost linear segment in the temperature range of 300–100 K and a power-law dependence prevailing between 100 and 10 K followed by a superconducting transition. The residual resistivity ratios (RRRs), defined as the ratio of the resistivity at 300 K to that at 10 K, are equal to 7.6 and 6 for the as-grown film and the patterned sample, respectively. The ZFC curves for α from 15° to 90° coincide within 4% with the ZFC curve for the structure with $\alpha = 0^\circ$ over the whole temperature range. This is a strong indication of the homogeneity of the transport properties of both Nb films from which all the structures

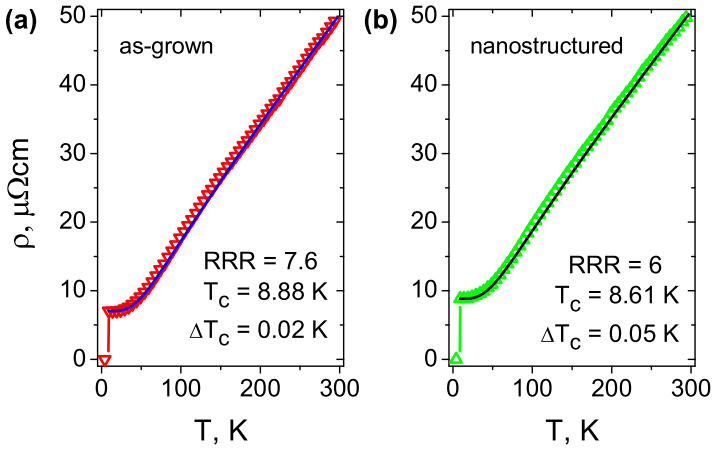

Figure 4. ZFC curves $\rho(T)$ for the as-grown film and the patterned sample with $\alpha = 0^\circ$. The corresponding fits by equation (2) are shown by solid lines.

are made. With increasing α from 0° to 90°, ρ grows monotonically. This rise originates from the nanostructuring and is caused by the reduction of the effective cross-section of the transport bridge due to the milled grooves.

We now turn to the comparison of the $\rho(T)$ curves for the as-grown film with that for the 0°-structure. At room temperature the resistivities of the patterned sample and the as-grown film are 50.4 and 49.9 $\mu\Omega$ cm, respectively. Both values are about a factor of 3 larger than the literature value for bulk Nb [48]. When the temperature decreases the difference between the $\rho(T)$ values increases. This is because the residual resistivity ρ_0 due to defect scattering in the patterned sample is about 20% larger than that for the as-grown film. The $\rho(T)$ curves can be fitted rather well by the Bloch–Grüneisen formula [49–51]

$$\rho(T) = \rho_0 + K(T/\Theta_D)^n \int_0^{\Theta_D/T} dx \frac{x^n}{(e^x - 1)(1 - e^{-x})}, \tag{2}$$

where Θ_D is the Debye temperature (275 K for Nb [48]), K is the only fitting constant and n is an integer determining the power law which in turn depends on the prevailing scattering mechanism in the sample. The fitting parameter K is chosen such that the best possible coincidence with the experimental curves in figure 4 is achieved for $\rho_{10\,K}$ and $\rho_{295\,K}$. Both curves $\rho(T)$ are fitted by equation (2) with $n = 5$, which implies that the resistance is due to scattering of electrons by phonons, as expected for nonmagnetic metals [51, 52].

Using the material constant for Nb, $\rho_0 l = 3.72 \times 10^{-6} \mu\Omega\,\text{cm}^2$ [53] and the values of $\rho_{10\,K}$ as 7.04 and 8.84 $\mu\Omega$ cm, the electron mean free path l can be estimated as 5.3 ± 0.3 and 4.2 ± 0.3 nm for the as-grown film and the patterned sample, respectively. The resistive properties of the samples are summarized in table 1. From the zero-field resistivity curves, one can conclude that the FIB processing noticeably changes the electrical transport properties of the nanostructured films. This is because of the implantation of Ga ions.

3.2. Hall effect

The transport properties of thin films are known to be sensitive to the degree of disorder and the carrier density in these films [54]. Whereas the degree of disorder chiefly changes the electron

Table 1. Transport properties of the samples in the normal state.

Sample	$R_{300\,K}$ (Ω)	$\rho_{300\,K}$ ($\mu\Omega$ cm)	$R_{10\,K}$ (Ω)	$\rho_{10\,K}$ ($\mu\Omega$ cm)	RRR	l (nm)	$R_{H10\,K}$ ($m^3\,C^{-1}$)	n (m^{-3})	T_c (K)	ΔT_c (K)	$B_{c2}(0)$ (T)	$\xi(0)$ (nm)
As-grown	32.7	49.9	4.36	7.04	7.6	5.3	7.71×10^{-11}	8.12×10^{28}	8.88	0.02	1.55	14.6
Patterned 0°	33.0	50.4	5.50	8.84	6	4.2	7.86×10^{-11}	7.95×10^{28}	8.61	0.05	1.9	13.2

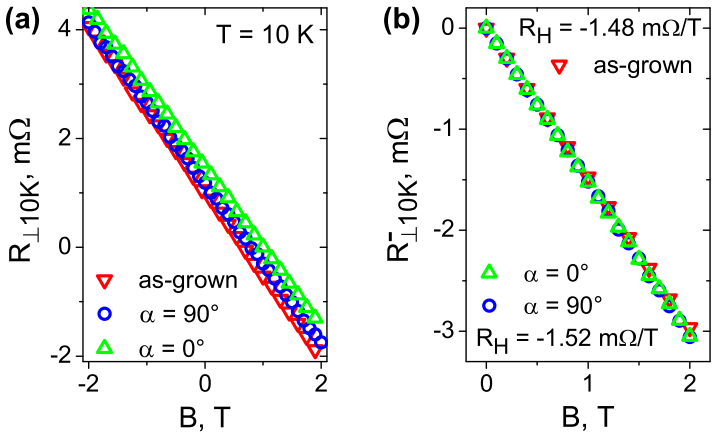

Figure 5. Transverse magneto-resistivity $R_\perp$ and its odd-in-field-reversal (Hall) component $R_\perp^-$ versus magnetic field B at 10 K for the non-structured and two nanostructured films, as indicated. The Hall coefficient R_H is obtained from the slope of the curves $R_\perp^-(B)$ by fitting a straight line.

mean free path, which has been deduced via the longitudinal resistivity, the carrier density can be directly calculated from Hall effect measurements. Figure 5 shows the transverse resistance $R_\perp$ recorded while sweeping the magnetic field from -2 to $+2$ T for the as-grown film and two patterned samples. The transverse odd-in-field-reversal (Hall) component $R_\perp^-$ for the same samples calculated by equation (1) is shown in figure 5(b). Considering the left graph first, it is seen that $R_\perp(B)$ for all the samples depends linearly on the field, as expected. All samples show a very small $R_\perp \neq 0$ at zero field. This appears as different vertical offsets of the straight lines of figure 5(a). This zero-field transverse resistance originates most likely from an unavoidable small misalignment of the oppositely arranged Hall leads. In some experiments [55], a balance bridge was used to compensate for this contribution. In other works, this offset is usually subtracted or the used leads are so narrow [56] that the misalignment error is very small with respect to the useful signal. In a recent work [57], it has been shown that an additional zero-field transverse voltage can arise solely due to a nonuniform transport current distribution in the sample. The effect has been predicted for both high-quality samples with a narrow and sharp superconducting transition and disordered samples with a wide transition, since only a minor transverse inhomogeneity is sufficient for its development. In general, the magnitude and details of this excess transverse voltage are unpredictable and hard to reproduce [57].

From the slope of the curve $R_\perp^-(B) = B/nqd$ we determine the Hall coefficient $R_H \equiv R_\perp^-(B)/B = 1/nqd$, where n is the carrier density, q is the electron charge and d is the

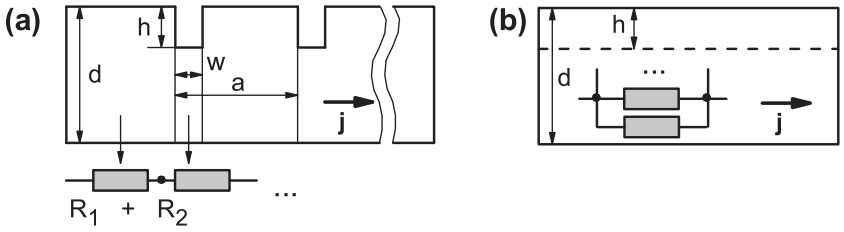

Figure 6. The equivalent electric schemes for the calculation of the normal-state resistivity anisotropy arising during the nanostructuring (a) for $\alpha = 90^\circ$ and (b) for $\alpha = 0^\circ$.

film thickness. The values of $R_H = 7.71 \times 10^{-11}\,m^3\,C^{-1}$ and $n = 8.12 \times 10^{28}\,m^{-3}$ are in good agreement with the previously reported values for Nb [58–60]. We note that n is reduced by 1–2% as a consequence of the nanostructuring. It is interesting to compare this value with the reduction of the valence electrons in the sample assuming that 5.5 at.% of 5-valent Nb have been replaced by 3-valent Ga. Such an estimate gives a reduction of 2.2%, which is rather close to the measured value.

3.3. Resistivity anisotropy

FIB milling alters the cross-section of the bridge. The changes in its magneto-resistivity can be used to find the relation between the number of beam passes for given beam parameters and the groove depth resulting from the nanoprocessing.

As a first case we consider $\alpha = 90^\circ$, i.e. the current of density j flows across the grooves (see also figure 6(a)). In our model, we assume that the sample is homogeneous, i.e. its thickness d and resistivity ρ are the same everywhere in the sample. We, moreover, assume that the FIB milling is 'ideal', i.e. the milled grooves have a rectangular cross-section and there is neither re-deposit of Nb nor Ga implants. Furthermore, we neglect the inhomogeneity of the current distribution in the plane of the sample caused by the milled grooves or the bridge edges or the contact leads. The sample is modeled by a $2n$-resistor network connected in series, where n is the number of grooves (see figure 6). In this network, we consider the cross-section between grooves giving the contribution R_1 in the total resistance R. The contribution R_1 does not depend on the groove depth h, while the cross-section under a groove gives us the h-dependent resistance R_2. Taking the geometry into account, it is sufficient, however, to consider just one pair of resistors R_1 and R_2. Both can be expressed in terms of the resistance of the pristine Nb film, R_{pr}, so that $R_{90} = R_{pr}(a-w)/a + R_{pr} \cdot w/a \cdot d/(d-h) = R_{pr}(1-k+zk)/(1-k)$, where $k = h/d$ and $z = w/a$. We obtain for $\alpha = 90^\circ$

$$R_{90}/R_{pr} = 1 + zk/(1-k). \tag{3}$$

When $\alpha = 0^\circ$ (see figure 6(b)), the resistances $R_1 = R_{pr}/(1-z)$ and $R_2 = R_{pr}/[z(1-k)]$, so that

$$R_0/R_{pr} = 1/(1-kz). \tag{4}$$

The relations given by equations (3) and (4) are plotted along with the *in-situ* recorded resistances in figure 1. The best possible coincidence with the experimental data in figure 1 has been achieved for the fitting parameter $z \equiv w/a = 1/7$. We note that the same value has

been obtained for the relative volume fraction $\varepsilon = 2b/a$ occupied by a real groove in section 2 (see figure 2(b)). Substituting $a = 420\,\text{nm}$ as a nanostructure period, one obtains $w = 60\,\text{nm}$ as the width of the rectangular-modeled grooves in figure 6. This value coincides within the experimental error with the full-width at half-depth of a groove $2b = 60 \pm 3\,\text{nm}$ deduced from the AFM-measured profile in figure 2(b). This means that for a simplified modeling, at least when h/d is relatively small, the real groove having a triangular-like cross section with the full-width at half-depth $2b$ can be treated as a rectangular-shaped groove with the width $w = 2b$. With $z = 1/7$, the experimental data can be fitted well by equations (3) and (4) up to about 23 000 passes, above which a knee-like deviation is observed. The most probable reasons for this are the ensuing nonuniform current distribution when $h/d \to 1$ or the unavoidable re-deposition of the milled material, which are not accounted for in our simple model. However, since our samples are patterned with $h/d \approx 15\%$ we believe that both effects are rather small in the present experiment. In particular, for a groove depth not exceeding 15% of the film thickness, we obtain in our work $\delta\rho \lesssim 3\%$, which is a factor of two smaller than that in [20].

Three important conclusions can be drawn from our analysis of the normal-state anisotropy so far: (a) it is shown both by modeling calculations and experimentally, that the normal-state resistivity anisotropy gives only a *small* contribution of $\delta\rho \leqslant 3\%$ to the resistive response in the normal state; (b) this anisotropy can be accounted for quantitatively; and (c) it does not hinder the observation and the proper analysis [41] of the anisotropic magneto-resistive response in the mixed state caused by the pinning anisotropy, which is discussed next.

4. Mixed-state properties

4.1. Superconducting transition

All the nanostructured samples are superconducting below a critical temperature of $T_c = 8.61\,\text{K}$, which is slightly reduced compared to that of the as-grown film for which it is 8.88 K. The critical temperature is determined as the temperature at which the resistivity has dropped to 90% of its extrapolated normal state value. The superconducting transitions for the different α are shown in figure 7(a). The spread in T_c for different nanostructured bridges is less than 5 mK. All the patterned structures demonstrate a sharp superconducting transition with a width ΔT smaller than 0.05 K. These are broader than $\Delta T \approx 0.02\,\text{K}$ for the unpatterned structure.

4.2. Upper critical field

The $\rho(T)$ dependences of all the samples were measured in a perpendicular field of up to 1.7 T. Figures 7(b) and (c) show the temperature dependence of the upper critical field $B_{c2}(T)$ determined as the respective onset of the $\rho(T)$ curves at a given B. Solid lines are the best fits by the standard expression [61] $B_{c2}(T) = B_{c2}(0)[1 - (T/T_c)^2]$ with the zero-temperature values $B_{c2}(0)$ for the as-grown film and the patterned sample with $\alpha = 0^\circ$ as 1.55 and 1.9 T, respectively. For $\alpha = 15^\circ$–90° the $B_{c2}(T)$ curves coincide with that for $\alpha = 0^\circ$ within 3% (not shown). Close to T_c the $B_{c2}(T)$ curves allow linear fits with slopes of $\mathrm{d}B_{c2}/\mathrm{d}T|_{T_c} = 0.24\,\text{T K}^{-1}$ and $\mathrm{d}B_{c2}/\mathrm{d}T|_{T_c} = 0.3\,\text{T K}^{-1}$ for the as-grown and the patterned sample, respectively. By using the approximate expression $B_{c2}(0) = 0.69 T_c \mathrm{d}B_{c2}/\mathrm{d}T|_{T_c}$ [54, 61], from the linear fits one obtains correspondingly $B_{c2}(0) = 1.47\,\text{T}$ and $B_{c2}(0) = 1.8\,\text{T}$, which are within 6% lower than the values obtained by the square-law expression.

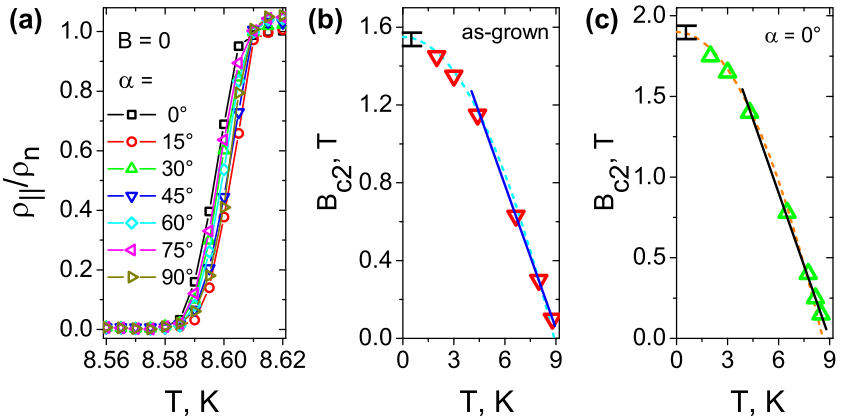

Figure 7. (a) Superconducting transition in zero magnetic field for different groove orientations with respect to the transport current direction, as indicated. (b) Temperature dependence of the upper critical field $B_{c2}(T)$ for the unpatterned structure. The $B_{c2}(0)$ value is estimated by fitting the standard expression $B_{c2}(T) = B_{c2}(0)[1-(T/T_c)^2]$ (dashed line). The linear fit in the range of $0.4T_c$–T_c is shown by a solid line. (c) The same as (b) but for the patterned structure with $\alpha = 0^\circ$. Error bars are also shown.

From the slopes $\mathrm{d}B_{c2}/\mathrm{d}T|_{T_c}$ we estimate the electron diffusion constant $D = -1.097(\mathrm{d}B_{c2}/\mathrm{d}T|_{T_c})^{-1}$ [62] as $4.57 \times 10^{-4}\,\mathrm{m^2\,s^{-1}}$ for the unpatterned sample and $3.66 \times 10^{-4}\,\mathrm{m^2\,s^{-1}}$ for the patterned sample, respectively. These values are comparable with the previously reported values for Nb films [63]. Below, these values will be used for the estimation of the Ginzburg–Landau (GL) depairing current at zero temperature.

4.3. Coherence length and magnetic penetration depth

From the expression $\xi(0) = [\Phi_0/2\pi B_{c2}(0)]^{1/2}$ [61], where $\Phi_0 = 2.07 \times 10^{-15}\,\mathrm{T\,m^2}$ is the magnetic flux quantum, the superconducting coherence length $\xi(0)$ for the as-grown film is 14.6 ± 0.3 nm and for the patterned sample it is 13.2 ± 0.3 nm. Having compared $\xi(0)$ with l, we conclude that regardless of the nanostructuring all the samples are in the dirty superconducting limit as $l < \xi(0)$. Accordingly, the nanostructuring does not change the relation between l and $\xi(0)$ in the as-grown and the processed samples qualitatively. For this reason, to calculate $\xi(T)$, we use the temperature-dependent relation for the dirty limit [61]

$$\xi(T) = 0.855[\xi(0)l]^{1/2}[1-T/T_c]^{-1/2}. \tag{5}$$

This dependence appears in figure 8, which illustrates how the two superconducting length scales (ξ and λ) vary with increasing temperature. In the same plot, the two nanostructure's lateral parameters (a and $2b$) are marked by horizontal lines for comparison. Note that the typical values of $2\xi(T)$ at $T \in [0.9T_c, 0.99T_c]$ are very close to the full-width at half-depth of the nanofabricated grooves $2b$. This allows us to conclude that in this temperature range the typical diameter of the vortex core is comparable with the lateral dimension of the groove where the superconducting order parameter is expected to be most suppressed. As a consequence of this, the grooves with such lateral dimensions are expected to behave as strong a pins which cause a pronounced anisotropic magneto-resistive response.

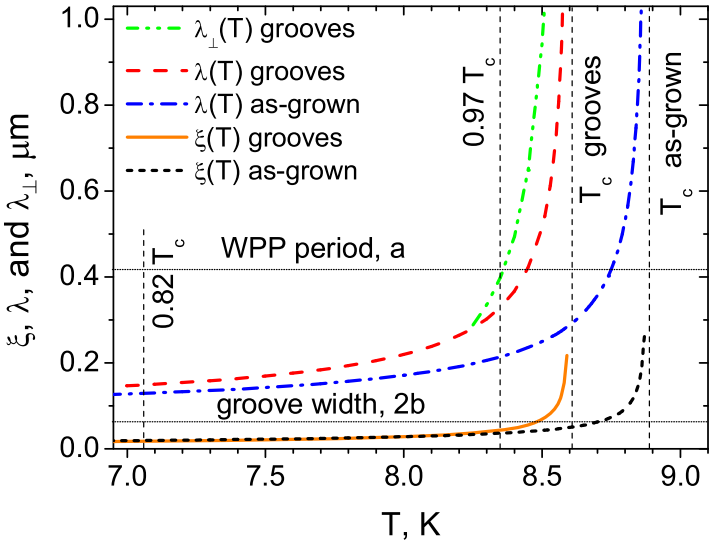

Figure 8. Temperature dependences of the superconducting coherence length calculated by the dirty-limit equation (5) and the magnetic field penetration depth by the empirical two-fluid model equations (6) and (7). For the as-grown and the nanostructured film, $\lambda(0)$ of 100 and 110 nm are used, respectively [53]. The horizontal lines mark two important nanostructure parameters, the full-width at half-depth of a groove $2b = 60$ nm and a nanostructure period $a = 420$ nm. The reduced temperature for the patterned sample is labeled close to the vertical dashed lines.

For completeness, from [53] we take the magnetic field penetration depth $\lambda(0)$ for a 52 nm-thick Nb film as 100 nm and use the Gorter–Casimir two-fluid approximation [61, 64]

$$\lambda(T) = \lambda(0)[1 - (T/T_c)^4]^{1/2}, \tag{6}$$

to plot $\lambda(T)$ in figure 8. As has been shown by Pearl [65], in a thin film for perpendicular field orientation the field fall-off is controlled not by λ but rather by a thickness-dependent $\lambda_\perp \approx \lambda_{\rm eff}^2/d \gg \lambda$, for which close to T_c [61]

$$\lambda_\perp(T) = \lambda_{\rm L}^2(T)[1 + 0.75\xi(0)/l]/d. \tag{7}$$

Substituting 39 nm [53, 66] for the London penetration length $\lambda_{\rm L}(0)$ at $T = 0$ K, the temperature dependence $\lambda_\perp(T)$ is shown in figure 8. It follows from the figure that for $T < 0.97T_c$ the value of $\lambda(T)$ is smaller than the nanostructure period a. Then, at accordingly small magnetic fields such vortices can be considered as virtually noninteracting. This validates the assumption of the *single-vortex approximation* which will be used for the theoretical modeling of more subtle phenomena in the vortex motion caused by the nanostructuring.

4.4. Critical current anisotropy

To determine the critical current density j_c different voltage criteria were used in the literature [6, 62, 67]. We use a 0.1 μV criterion. The reduction of this criterion does not significantly affect the results but the contribution of noise becomes more pronounced. The measurements were conventional dc steady-current-sweep measurements. Zero-field values

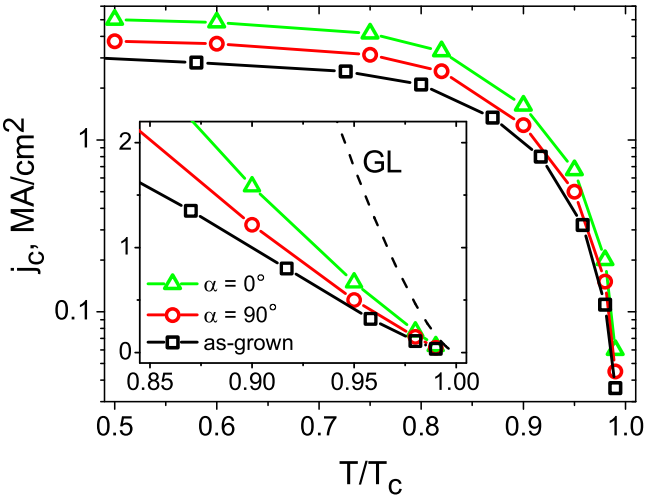

Figure 9. The temperature dependence of the zero-field critical current density $j_c(T)$ for the as-grown film and the two patterned samples, as indicated. The inset shows a zoomed-in range $0.85 < t < 1$ where the GL depairing current is shown by a dashed line.

of j_c deduced from the current–voltage characteristics (CVCs) at a series of temperatures are shown in figure 9. The transitions into the normal state are very sharp and for $0.7T_c \lesssim T < 0.99T_c$ they are non-hysteretic while sweeping the current up or down, so that the inaccuracy of the data shown is less than 2%. For lower temperatures, $0.5T_c < T \lesssim 0.7T_c$, the data in figure 9 are those $j_c(T)$ values deduced when the current sweeps up. We consider the analysis of overheating effects and the hysteretic behavior of $j_c(T)$ as beyond the scope of our discussion, as the central results of our work refer to only those data which were acquired out of the temperature range where these effects are important.

We next compare the measured data with the temperature dependence of the GL depairing current [68]

$$j_c^{GL}(T) = j_c^{GL}(0)(1-t^2)^{3/2}(1+t^2)^{1/2},$$
$$\text{where } j_c^{GL}(0) = 4.53(k_B T_c)^{3/2}/(e\rho\sqrt{D\hbar}) \tag{8}$$

is the zero-temperature critical current density and $t = T/T_c$ is the reduced temperature. From the measured $\rho_{10\,K}$ value and the calculated D we estimate $j_c^{GL}(0) \simeq 45\,\text{MA cm}^{-2}$ for all samples. Experimentally, the $j_c(t)$ curves level off at one order of magnitude smaller values. This is because of the omnipresence of vortices, which under the current action are set in motion resulting in dissipation. Only if there were no vortices or they were (ideally) completely pinned could the measured critical current density reach the depairing value. In accordance with [69], in order to completely exclude vortices from a superconductor sample, its width W must be smaller than $4.4\xi(T)$. As a consequence, the GL critical current can be measured in a wide temperature range only if the bridge width is in the few hundreds of nm range in the case of Nb films [70]. In the present experiment, the condition $W < 4.4\xi(T)$ ($W = 30\,\mu$m) can be satisfied only in a very narrow temperature range when $\xi(T)$ diverges at $T - T_c \ll T_c$. The inset of figure 9 shows that the values of $j_c(T)$ measured not very close to T_c lie well below the GL curve.

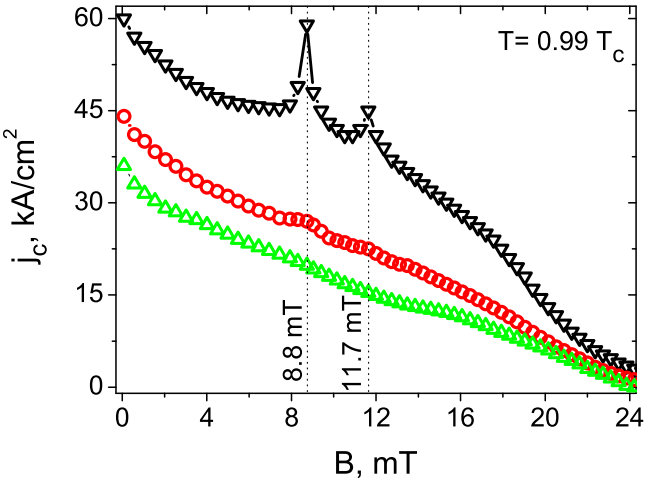

Figure 10. The field dependence of the critical current $j_c(B)$ for the as-grown ($\triangle$) and the nanostructured samples with $\alpha = 0^\circ$ ($\triangledown$) and $\alpha = 90^\circ$ ($\bigcirc$). The two matching fields are shown by vertical dotted lines.

Important for the following discussion is the critical current close to T_c, $j_c(0.99T_c) \simeq 50\,\mathrm{kA\,cm^{-2}}$. Apparently, the j-values of 0.7 and $6.4\,\mathrm{kA\,cm^{-2}}$ routinely used in the resistivity measurements are small with respect to j_c. Therefore, it is safe to assume that not very far from T_c the experiment is carried out in the absence of possible electron overheating [71, 72] and pair-breaking effects. In other words, the experiment is carried out in the weak-current limit, which allows us to perform an Arrhenius analysis of $\rho(T)$ in order to determine the pinning activation energy. Finally, let us turn to the selection of specific magnetic field values at which a major part of the resistivity data will be acquired.

4.5. Matching fields

The $j_c(B)$ dependences for all samples were deduced from the CVCs by employing the same criterion of a voltage drop of 0.1 μV measured in different small perpendicular fields. The data thus obtained at $0.99T_c$ are presented in figure 10.

Let us consider first the $j_c(B)$ curves of the as-grown film for reference purposes. The $j_c(B)$ dependence is a decreasing function of B with a steeper descent at very small magnetic fields, quasi-linear behavior in the field range of 3–24 mT and tending to zero at higher fields. The steeper decrease in $j_c(B)$ at 0–1 mT can be associated with a very small lower critical magnetic field value $B_{c1}(T)$ and the penetration of Abrikosov vortices into the sample such that their motion leads to the appearance of a finite voltage drop already at a very small transport current. One can also distinguish a smooth 'shoulder' in $j_c(B)$ between 15 and 19 mT. If one takes an average field of 17 mT, then, in accordance with the relation $a_\triangle = 0.5\sqrt{3\Phi_0/B}$ for a triangular vortex lattice, some spatial inhomogeneity with a characteristic length close to 300 nm must be the reason for this. An indication of the origin of this shoulder can be found from a close inspection of AFM images taken from the sapphire substrates [44]. We find that the average step edge distance between two neighboring miscut terraces has about the same length scale. These step edges are known to serve as nucleation sites for adatoms during the film deposition [47]. Overgrown Nb films are known to replicate these terraces [73, 74]. Hence, it is possible that the

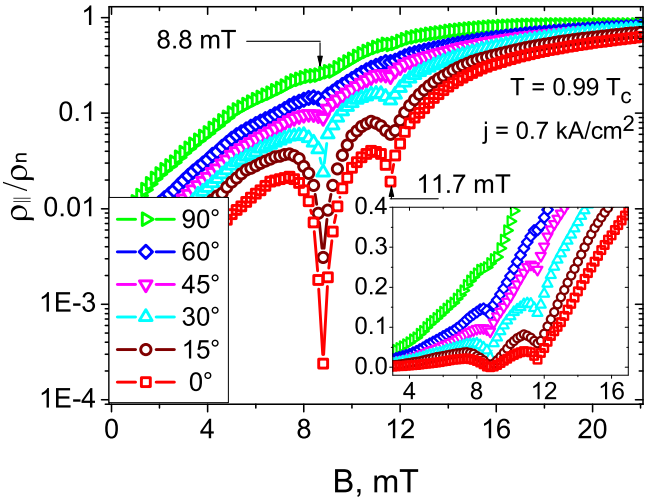

Figure 11. Field dependence $\rho_{\parallel}(B)$ at $0.99T_c$ for a current density of $j = 0.7\,\mathrm{kA\,cm^{-2}}$ and different α, as indicated. The inset shows $\rho_{\parallel}(B)$ in linear scale.

order parameter in the films is slightly modulated with the same characteristic length scale and thereby provides this smoothed enhancement of $j_c(B)$ at 15–19 mT. Additional evidence for the validity of this assumption is that this 'shoulder' is observed in $j_c(B)$ for the as-grown as well as for the nanostructured samples regardless of α.

The $j_c(B)$ curves for the samples with grooves differ substantially from that for the as-grown film. Even for the case when a transport current flows across the grooves ($\alpha = 90°$) and these grooves practically do not hinder the vortex motion along them, the critical current values are a factor of 1.3 higher than those for the non-structured sample up to 15 mT and tend to approach $j_c(B)$ of the as-grown film above 15 mT. This means that a larger amount of uncorrelated disorder is present in the patterned samples with respect to the as-grown film. Two additional features in the $j_c(B)$ curve are developing as α is reduced from 90° to 0°. One is that j_c acquires larger values at zero field so that the ratio $j_c(0°)/j_c(90°)$ grows to a value of 1.36. Another is the appearance of two sharp maxima at fields of 8.8 and 11.7 mT. The peak magnitude is maximal when $\alpha = 0°$ so that $j_c(0°, 8.8\,\mathrm{mT})$ is almost equal to $j_c(0°, 0)$. The maximum at 8.8 mT is more pronounced than that at 11.7 mT. Assuming a triangular vortex lattice, the peaks correspond to a vortex–vortex distance of $a_{\triangle} = 485$ and 420 nm, respectively. The presence of more than one matching field has been previously reported for a complementary pinning landscape in the form of deposited Co lines [39]. However, most likely due to the smoothed pinning potential profile in that work [39], the matching peculiarities were less pronounced than reported in the present case.

To investigate the features arising from the nanostructuring with a higher resolution in field, all the patterned samples were subjected to direct measurements of $\rho(B)$ at a very small dc current density of $0.7\,\mathrm{kA\,cm^{-2}}$. The results for $T = 0.99T_c$ are presented in figure 11. All the $\rho(B)$ curves are nonlinear increasing functions of the field and saturate to the normal-state resistivity values at about 35 mT. With a decrease of α from 90° to 0°, two pronounced minima are developing. The minimum occurring at 8.8 mT exhibits a characteristic drop of two orders of magnitude, whereas the drop at 11.7 mT is much less pronounced, so that $\rho(B)$ is reduced

by only about a factor of 2. Taking into account the observed peculiarities in both dependences, $j_c(B)$ and $\rho(B)$, we argue that the best geometrical matching between the vortex ensemble and the underlying structure is achieved at a field of 8.8 mT, which represents the first (fundamental) matching field [39].

5. Quantification of pinning

5.1. Experimental parameters

We now turn to a thorough analysis of the temperature dependences of the magneto-resistive response measured for the different α in the patterned samples. A transport current of a small density 6.4 kA cm^{-2} was chosen for this type of measurement. Selected measurements were repeated for 0.7 kA cm^{-2}. The temperature range of 7.06–8.61 K ($0.82T_c$–T_c) was sampled. The fields B of 5, 8.8, 10, 11.7 and 15 mT, much lower than the upper critical field $B_{c2}(T, j)$, were used. Assuming a triangular vortex lattice, the field values were selected from figures 10 and 11 in such a way that the vortices are made to arrange in different configurations with respect to the underlying pinning landscape. These correspond to three qualitatively different cases (denoted by the indexes 'a', 'b' and 'c' in the following): firstly, the field of $B_a = 8.8$ mT corresponds to the fundamental matching field, i.e. when all the vortices are pinned at the bottom of the grooves and there are no interstitial vortices. Secondly, a field of $B_b = 11.7$ mT represents the secondary matching field at which half the total number of vortices are pinned at the groove bottoms and the remaining vortices are pinned by randomly distributed isotropic (i) pins in between. We will refer to this field as the field of partial matching. Finally, a field of $B_c = 15$ mT is selected as representative of a mismatching field, i.e. when a major fraction of vortices is interstitial. About six interstitial vortices per vortex pinned to a groove can be taken as a rough estimate of this vortex lattice configuration.

5.2. Angle-dependent magneto-resistive response

The behavior of $\rho_{\parallel}^{+}(T)$ for different α and B values differs substantially. The curves in figures 12(a)–(c) show very good systematic behavior in α and qualitatively resemble those measured on thin Nb films grown by molecular beam epitaxy on facetted sapphire substrates in [20]: the smoothed step-like curves $\rho_{\parallel}^{+}(T)$ are clearly anisotropic and their shape strongly depends on the angle α. In the limiting case of the vortices moving along the grooves, i.e. for $\alpha = 90^{\circ}$, the vortices are influenced only by the i pinning sites. Since a pins are not effective in impeding this motion, the dissipation is pronounced and this is why a nonzero resistance 'tail' is observed. The longer this 'tail' the weaker the i pinning is. In the opposite limiting case, when the grooves effectively pin the vortices, the superconducting state is preserved up to higher temperatures. When the temperature is increased, the vortices, finally, are thermally activated from the grooves and the resistive transition in this case is most sharp. For intermediate α, with increasing temperature, the vortex movement consequently changes its character from a thermally activated motion to that of viscous flux flow with respect to both the i and a pinning potentials. With increasing magnetic field, the step-like transitions become smoother, as expected. In order to quantify the pinning potential parameters we now turn to an Arrhenius analysis of the even longitudinal resistivity component $\rho_{\parallel}^{+}(T)$.

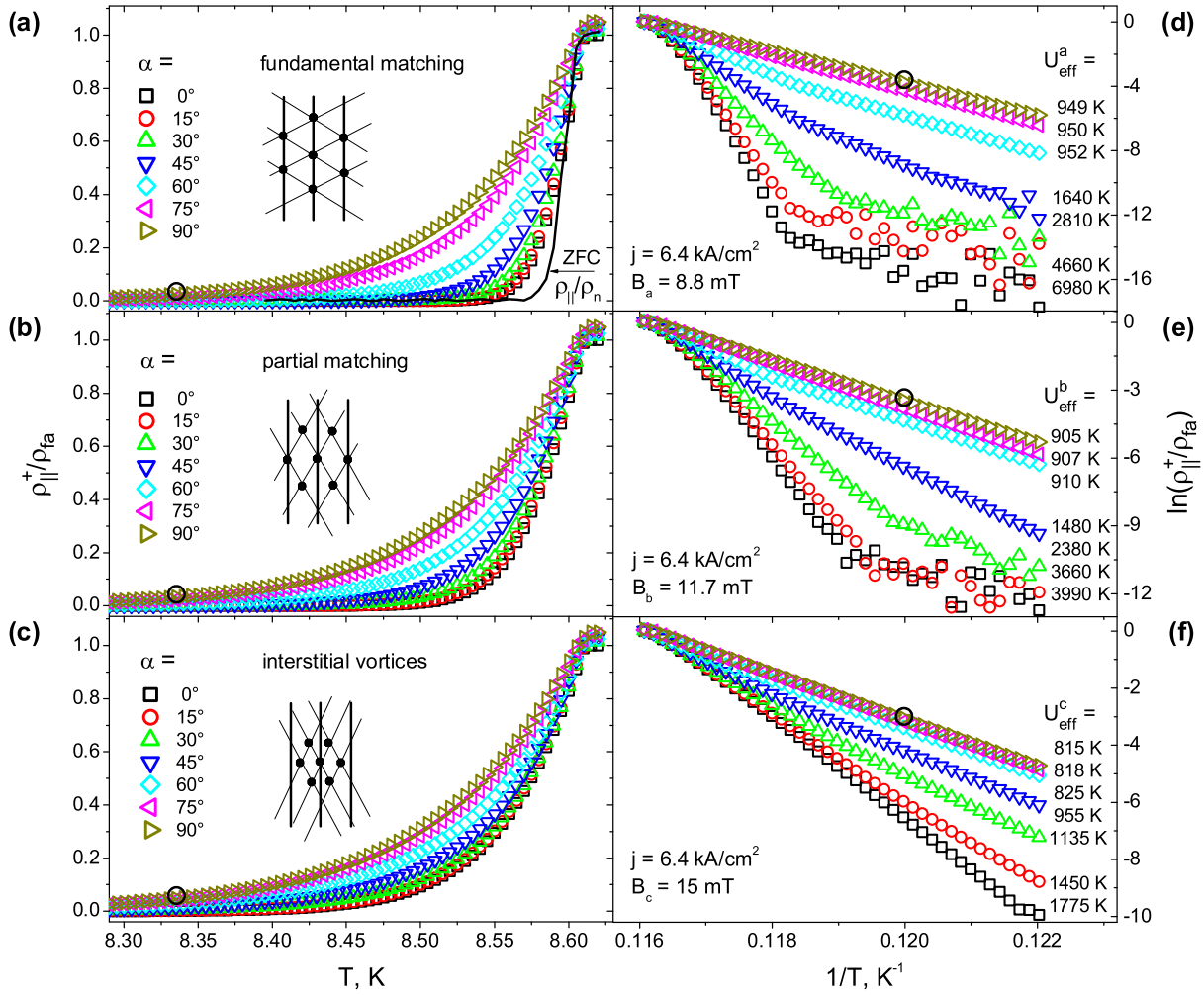

Figure 12. The temperature dependence of the even longitudinal magnetoresistivity component $\rho_{\parallel}^{+}(T)$ for the different grooves orientation with respect to the transport current, as indicated. The data are collected in a magnetic field of (a) $B_{\mathrm{a}} = 8.8\,\mathrm{mT}$ corresponding to the fundamental matching field, (b) $B_{\mathrm{b}} = 11.7\,\mathrm{mT}$ being the partial matching field and (c) $B_{\mathrm{c}} = 15\,\mathrm{mT}$ as representative of interstitial vortices. All the curves (a)–(c) are normalized by the flux-flow resistivity $\rho_{f\mathrm{a}} = \rho_{\mathrm{n}} B_{\mathrm{a}}/B_{\mathrm{c2}}(T)$ to augment the difference in their behavior. The ZFC curve for $\alpha = 0^{\circ}$ normalized by ρ_{n} is shown in panel (a) by a solid line for comparison. The corresponding vortex lattice configurations are shown schematically in the insets. The corresponding Arrhenius plots $\ln[\rho_{\parallel}^{+}/\rho_{f\mathrm{a}}](1/T)$ with the deduced activation energies U_{eff} labeled close to the curves are shown in panels (d)–(f). Black circles show the temperature point in the linear parts of the Arrhenius plots used for the exemplary calculation of U_{eff}^{0} in the text.

5.3. Arrhenius analysis

It is well known [4, 75, 76] that in the limit of small current density the vortex motion in a pinning potential is of thermally activated character. Thus, an Arrhenius analysis can be applied

to the temperature dependences of the even longitudinal magneto-resistivity $\rho_{\parallel}^{+}$ in order to estimate the activation energy produced by the pinning barriers for the vortex motion.

The Arrhenius analysis relies upon the assumption that the resistivity of the sample is independent of the transport current and is given by Arrhenius law

$$\rho = \rho_0 \exp \frac{-U_{\mathrm{eff}}}{k_{\mathrm{B}} T}, \tag{9}$$

where ρ_0 is a constant and U_{eff} is the effective activation energy. Then, if one plots ln ρ versus the inverse temperature T^{-1} and this curve can be fitted by a straight line, which is the fingerprint of the thermo-activated character, the slope of the linear part of the Arrhenius plot gives directly the activation energy U_{eff}. The Arrhenius plots are shown in figures 12(d)–(f). The corresponding activation energies for the different α values are labeled close to the curves.

From the Arrhenius plots, one can see that the pinning anisotropy in the mixed state plays a much more important role than the resistivity anisotropy of the patterned sample in the normal state. The curves practically coincide in the left part of the Arrhenius plots, which corresponds to the normal state, whereas in the superconducting state their behavior is strongly dependent on the groove orientation with regard to the transport current direction. For a complete account of the resistivity data analysis with the help of Arrhenius' treatment, see [20]. Performing calculations in the spirit of that work [20], here we show only the main results of this analysis.

We use the stochastic model of the nonlinear single-vortex dynamics under the competing i and a pinning conditions [20, 32]. In the weak-current limit, for the analysis of ln $\rho_{\parallel}^{+}(T)$ the following model function for both pinning potentials is used:

$$\nu(T, F) = \exp \frac{-\theta U_{\mathrm{eff}}}{k_{\mathrm{B}} T}, \tag{10}$$

where $\theta = 1 - T/T_{\mathrm{c}}$ is the normalized deviation from the critical temperature. The effective pinning potential is given by $U_{\mathrm{eff}} = U_0 - Fb$ with U_0 the depth of the potential well. F is the external force acting on the vortex and b is the characteristic width of the pinning potential. In general, both probability functions ν_i and ν_a can be represented by relation (10) with different parameters U_{0i}, U_{0a}, b_i and b_a and variables F_i and F_a. The quantities related to i and a pinning are denoted by the appropriate subscripts. The functions ν_i and ν_a have the physical meaning of the probability of overcoming the effective potential barrier of the corresponding pinning potential.

Previously it has been shown how the general expression for $\rho_{\parallel}^{+}(T)$ can be simplified for certain limiting cases (see equation (42) of [20]). In particular, for two different nanostructure orientations for large enough α and low temperatures, one can estimate the value of the term Fb_i and the depth of the i pinning potential well U_{0i} by solving the system of equations

$$\begin{aligned} Fb_i &= [U_{\mathrm{eff}}(\alpha_1) - U_{\mathrm{eff}}(\alpha_2)]/[\sin\alpha_2 - \sin\alpha_1], \\ U_{0i} &= [U_{\mathrm{eff}}(\alpha_1)\sin\alpha_2 - U_{\mathrm{eff}}(\alpha_2)\sin\alpha_1]/[\sin\alpha_2 - \sin\alpha_1]. \end{aligned} \tag{11}$$

In particular, let us consider the Arrhenius plot in figure 12(d) for $B_{\mathrm{a}} = 8.8$ mT. For two different angles $\alpha_1 = 90^\circ$ and $\alpha_2 = 60^\circ$ we take the corresponding $U_{\mathrm{eff}}^{\mathrm{a}}(90^\circ)$ from figure 12(d) as 949 K and $U_{\mathrm{eff}}^{\mathrm{a}}(60^\circ) = 952$ K. Then, from equation (11), one obtains $Fb_i^{\mathrm{g}} \approx 22$ K. Here and in the following, the index 'g' denotes that this value relates to the i pinning at the groove bottoms. If the transport current flows perpendicular to the magnetic field, the Lorentz force F acting on the vortex can be estimated using $F = (\Phi_0/c) j l_{\mathrm{g}}$, where $j = 6.4\,\mathrm{kA\,cm^{-2}}$ is the density of the transport current. Since for $B_{\mathrm{a}} = 8.8$ mT all the vortices are pinned at the groove bottoms,

Table 2. Left panel: the activation energies $U_{\rm eff}$ in the patterned structures for the different α and in the unpatterned reference film. The values are deduced from the corresponding Arrhenius plots in figures 12 and 13, respectively. The notions 'fundamental matching', 'partial matching' and 'interstitial vortices' relate to the patterned structures only. Right panel: the calculated width b and depth U_0 of the pinning potentials. The i pinning stemming from the nanostructuring is quantified at the groove regions and between the grooves. The background i pinning in the unpatterned sample originates from disorder occurring during the film growth.

Patterned structures	Fundamental matching $B_{\rm a} = 8.8$ mT	Partial matching $B_{\rm b} = 11.7$ mT	Interstitial vortices $B_{\rm c} = 15$ mT
α (deg)	$U_{\rm eff}^{\rm a}$ (K)	$U_{\rm eff}^{\rm b}$ (K)	$U_{\rm eff}^{\rm c}$ (K)
0	6980	3990	1775
15	4660	3660	1450
30	2810	2380	1135
45	1640	1480	955
60	952	910	825
75	950	907	818
90	949	905	815
Unpatterned film	753	750	747

Calculated pinning potential parameters	
a pinning	$U_{0a} \approx 6010$ K
	$b_a = 210$ nm
i pinning at the groove bottoms	$U_{0i}^{\rm g} \approx 970$ K
	$b_i^{\rm g} \approx 50$ nm
i pinning between the grooves	$U_{0i}^{0} \approx 830$ K
	$b_i^{0} \simeq 50$–100 nm
i pinning in the unpatterned film	$U_{0i}^{\rm ref} \simeq 760$ K
	$b_i^{\rm ref} \simeq 100$ nm

$l_{\rm g} \approx 0.85d$ must be taken for the vortex length instead of the full thickness of the Nb film. Then, one obtains that $b_i^{\rm g} \approx 50$ nm. From equation (11), the corresponding depth of the i pinning potential at the groove bottoms $U_{0i}^{\rm g} \approx 970$ K. Performing the same analysis for $j = 0.7$ kA cm^{-2}, the pinning parameters coincide with those obtained above within an error of 7%. The most important values are summarized in table 2.

To estimate the a pinning parameters it is supposed that the pinning potential width b_a corresponds to half the period of the nanostructure, i.e. $b_a = 210$ nm. Thus, the product Fb_a can be estimated as $\approx$90 K. The fact that both products, $Fb_i^{\rm g}$ and Fb_a, are much smaller than all measured activation energies $U_{\rm eff}$ in table 2 underlines that the experiment is indeed performed in the weak-current limit. For the estimation of the depth of the potential well U_{0a} the Arrhenius plot for $\alpha = 0^\circ$ is considered. It has been previously shown [20] that $U_{\rm eff}^{\rm a} \approx U_{0a} + U_{0i}^{\rm g}$ in this case. The thus obtained value is $U_{0a} \approx 6010$ K.

The same analysis scheme cannot be directly employed to treat the $\rho_\parallel^+(T)$ dependences at 11.7 and 15 mT. In these cases, the numbers of vortices pinned by grooves and those pinned in between them must be appropriately taken into consideration. This includes also the difference in the vortex lengths and, consequently, the difference in the driving forces acting on the vortices. Besides, the quantitative calculation of the pinning parameters in these cases is a rather complex problem. The most crucial issues arising in this regard are reported, e.g., in [77]. These include the coexistence of (temporarily) pinned vortex domains moving with different correlation lengths of the vortex lattice, dependent on the relative strength of pinning, driving force and the vortex–vortex interaction. Consequently, a complete quantitative analysis of all

these phenomena is out side the scope of this work. Nevertheless, we would like to perform a simplified analysis of the plots in figures 12(b) and (c) for $\alpha = 90^\circ$, i.e. when vortices experience only i pinning. In our treatment, we neglect vortex–vortex interactions and do not distinguish the vortex viscosity for the vortices moving at the groove bottoms from the viscosity for their movement between the grooves. We, moreover, assume that T_c is the same in the groove regions and between them. Below, the index '0' will be used for the values related to the vortices moving between the grooves. Then, the resistivity can be written as follows:

$$\rho_{\parallel}^{+}(T) \equiv \rho_f \nu(T) = [\rho_{fg} n_g \nu_g(T) l_g/d + \rho_{f0} n_0 \nu_0(T)], \tag{12}$$

where n_g and n_0 are the relative numbers of vortices moving at the groove bottoms and between the grooves, respectively. The flux-flow resistivities are $\rho_{fg} = B_g \Phi_0/\eta_g c^2$ and $\rho_{f0} = B_0 \Phi_0/\eta_0 c^2$. In the following, we use that $B_g = B_0$ and assume that $\eta_g = \eta_0$. In equation (12), $l_g \approx 0.85d$ stands for the film thickness at the groove bottoms.

Next, we choose a temperature point in the linear parts of the Arrhenius plots in figures 12(d)–(f), e.g. $1/T = 0.12\,\mathrm{K}^{-1}$ ($T = 8.333\,\mathrm{K}$). From the experimental curves in figure 12(b) for $B_b = 11.7\,\mathrm{mT}$ we obtain $\nu_b = 0.038$. Then, having substituted $n_g = n_0 = 0.5$ in equation (12), the pinning activation energy for the interstitial vortices is $U_{\mathrm{eff}}^0 \approx 800\,\mathrm{K}$. For $B_c = 15\,\mathrm{mT}$ the appropriate fractions of vortices are $n_g = 0.15$ and $n_0 = 0.85$, and $\nu_c = 0.047$ from figure 12(f) can be taken. Then, the almost identical value of $U_{\mathrm{eff}}^0 \approx 805\,\mathrm{K}$ ensues for the interstitial vortices. Taking the values of ν_b and ν_c for a set of other temperatures in the range of 7–8.4 K (not shown), we obtain $U_{\mathrm{eff}}^0 \approx 800\,\mathrm{K}$. Note that U_{eff}^0 for the interstitial vortices is smaller than $U_{\mathrm{eff}}^c \approx 815\,\mathrm{K}$ for the whole vortex system in figure 12(f), as is reasonable. In this way, the activation energy for $\alpha = 90^\circ$ is noticeably decreasing (see table 2) with an increase of the field from 8.8 mT up to 15 mT. As a result, the depth of the i pinning potential U_{0i} is decreasing from its value at the groove bottoms, where it is $U_{0i}^g \approx 970\,\mathrm{K}$, to the value of $U_{0i}^0 \approx 830\,\mathrm{K}$ between the grooves. The last value is probed when the vortex lattice no longer matches the underlying nanostructure and an increasing number of interstitial vortices appear. This is most likely accompanied by an increase of the period $b_i^0 \simeq 50$–$100\,\mathrm{nm}$ of the i pinning potential along with the reduction of the concentration of i pins out of the groove regions.

For the unpatterned reference sample (see figure 13), a pinning activation energy of $U_{\mathrm{eff}}^{\mathrm{ref}} \approx 750\,\mathrm{K}$ is deduced. Using the current density of $j = 0.7\,\mathrm{kA\,cm}^{-2}$, the film thickness of $d = 52\,\mathrm{nm}$ and the pinning potential width of $b_i^{\mathrm{ref}} \simeq 100\,\mathrm{nm}$, the term $F b_i^{\mathrm{ref}}$ can be estimated as $\simeq 10\,\mathrm{K}$. Accordingly, $U_{0i}^{\mathrm{ref}} \simeq 760\,\mathrm{K}$ for the as-grown film. Note that b_i^g in the patterned sample is a factor of two smaller than b_i^{ref}. Consequently, in the unpatterned reference sample uncorrelated disorder is less pinning active and the concentration of i pins is smaller with respect to the patterned sample even if the i pinning between the grooves is compared. Based on these findings and taking into account the processes occurring during the nanostructuring, we conclude the presentation of our results with a discussion of all possible mechanisms which are relevant for the enhancement of pinning in the nanostructured samples.

5.4. Mechanisms of pinning enhancement in nanostructured films

Let us first compare the calculated pinning parameters with the values known from the literature. For instance, the activation energy for the vortex motion across twinning planes in high-temperature superconductors is of the order of 1000 K [76]. In Nb films grown by molecular beam epitaxy on facetted sapphire substrates, this value is between 1600 and 4000 K [20]. Accordingly, in the present experiment from the activation energies it appears that the fabricated

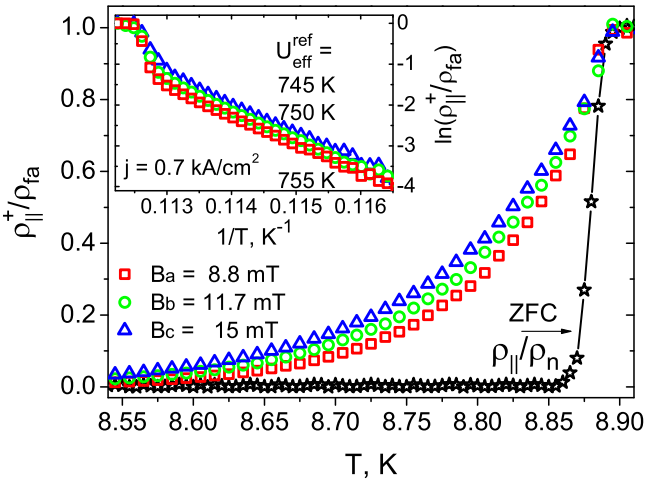

Figure 13. The temperature dependence of the even longitudinal magnetoresistivity component $\rho_{\|}^{+}(T)$ for the unpatterned film at a set of magnetic fields, as indicated. The data are collected at a current density j of 0.7 kA cm^{-2}. The curves are normalized by the flux-flow resistivity $\rho_{fa} = \rho_n B_a / B_{c2}(T)$ to augment the difference in their behavior. The ZFC curve normalized by ρ_n is shown for comparison. Inset: the corresponding Arrhenius plots $\ln[\rho_{\|}^{+}/\rho_{fa}](1/T)$ with the deduced activation energies U_{eff}.

grooves act as very strong *a* pins. At the same time, background *i* pinning is revealed to be weaker than that in [20]. As a consequence of this, the anisotropic effects are clearly visible.

The relative weakness of *i* pinning in the present work can be attributed to two factors: (i) due to the non-perfect periodicity [35] of the facetted surface in [20], *i* pinning was probed simultaneously in the alternating facet slopes and ridges. (ii) In this work, the film used is a factor of 2 thicker and thus the thickness-induced suppression of the superconducting order parameter must be smaller. Due to the possibility of selecting the most likely pinning sites for the vortices, pinning in different regions of the samples could be probed (see figure 14). A slight alteration of the amount of Ga and thus a slight suppression of the superconducting order parameter along the grooves' bottom is the reason for the somewhat enhanced pinning by point-like disorder when a vortex is guided by a groove.

Finally, we provide arguments why *a* pinning caused by the grooves is so strong. We suppose four different mechanisms which drive the vortices towards groove pinning. Firstly, the reduction of the length of a vortex being pinned by a groove renders pinning more effective there due to vortex energy reduction. Secondly, Ga implants stopped in the sample underneath the milled groove provide strong pins. Thirdly, additional sources of pinning are provided by the amorphization of and the vacancy generation in Nb caused by the Ga ion bombardment. Finally, the superconducting order parameter is suppressed due to the reduced film thickness at the position of the grooves. All these mechanisms have the same effect and cause a rather strong *a* pinning potential. In principle, the strength of *a* pinning can be increased even further. However, one has to consider that the normal-state resistive response will then be more strongly anisotropic and the inhomogeneity of the transport current distribution will be more pronounced in this case.

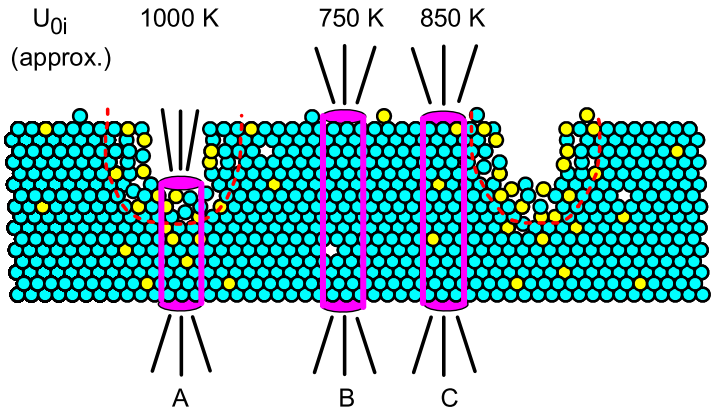

Figure 14. Out-of-scale representation of the changes in the structural and the associated pinning properties of the samples invoked by FIB milling. Cyan circles correspond to Nb atoms, yellow ones to Ga implants and the background point-like disorder is shown by empty circles. Dashed lines mark the amorphous area. Solid cylinders illustrate magnetic vortices pinned by different parts of the sample: vortex A is pinned by a groove. The groove acts as a strong a pin for any $\alpha \neq 90^\circ$. For $\alpha = 90^\circ$, the groove provides the enhanced i pinning. Note the vortex length reduction. Vortex B experiences the virtually unchanged i pinning occurring during film growth. Vortex C probes the enhanced i pinning caused by Ga implants during the nanostructuring. To present a qualitative picture, the depths of the i pinning potential wells are indicated approximately.

6. Conclusion

We have studied the influence of the direct nanoprocessing by FIB milling on the material composition, magneto-transport and pinning properties of epitaxial Nb(110) thin films via electrical dc transport measurements. The main results can be formulated as follows: (i) the employed nanoprocessing has been revealed to change both the normal-state and the mixed-state properties of the samples, by means of Ga implants in the patterned structures. The interrelated changes in the structure and the magneto-resistive properties of the FIB-patterned Nb films have been analyzed. (ii) The normal-state resistivity anisotropy has been shown to be small, amounting to less than 5% of the normal-state resistivity. The changes in the samples' resistivity during the nanostructuring have been accounted for quantitatively and allowed for a calibration of the pre-defined groove depth for given FIB milling parameters. (iii) The pinning anisotropy in the mixed state has been found to be much more pronounced than the resistivity anisotropy in the normal state. Two matching fields have been observed for the vortex lattice with the underlying pinning potential nanolandscape. The magneto-resistive response has been shown to be most anisotropic for the fundamental matching field. (iv) The pinning potential parameters for Nb films with FIB-milled WPP nanostructures have been quantified and will be used in a forthcoming work [41] for the comparison of the experiment with the theory. By providing a deeper insight into the pinning enhancement mechanisms at work in FIB-patterned superconductors, we hope to stimulate further research along this line.

Acknowledgments

Roland Sachser is acknowledged for the software written and his help with the *in situ* measurements. OVD gratefully acknowledges financial support from the Deutsche Forschungsgemeinschaft through grant no. DO 1511/2-1. EB acknowledges the Beilstein-Institut, Frankfurt/Main, Germany, for financial support within the research collaboration NanoBiC. VAS acknowledges partial financial support under grant agreement no. PIRSES-GA-2009-247556.

References

[1] Moshchalkov V V and Fritzsche J 2011 *Nanostructured Superconductors* (Singapore: World Scientific)
[2] Silhanek A V, Van de Vondel J and Moshchalkov V V 2010 Guided vortex motion and vortex ratchets in nanostructured superconductors *Nanoscience and Engineering in Superconductivity* (Berlin: Springer) chapter 1, pp 1–24
[3] Plourde B L T 2009 *IEEE Trans. Appl. Supercond.* **19** 3698–714
[4] Blatter G, Feigel'man M V, Geshkenbein V B, Larkin A I and Vinokur V M 1994 *Rev. Mod. Phys.* **66** 1125–388
[5] Brandt E H 1995 *Rep. Prog. Phys.* **58** 1465
[6] Pautrat A, Scola J, Goupil C, Simon C, Villard C, Domengès B, Simon Y, Guilpin C and Méchin L 2004 *Phys. Rev.* B **69** 224504
[7] Peroz C and Villard C 2005 *Phys. Rev.* B **72** 014515
[8] Liang M, Kunchur M N, Hua J and Xiao Z 2010 *Phys. Rev.* B **82** 064502
[9] Reichhardt C, Olson C J and Nori F 1997 *Phys. Rev. Lett.* **78** 2648–51
[10] Kokubo N, Besseling R and Kes P H 2004 *Phys. Rev.* B **69** 064504
[11] Kokubo N, Asada T, Kadowaki K, Takita K, Sorop T G and Kes P H 2007 *Phys. Rev.* B **75** 184512
[12] Grimaldi G, Leo A, Nigro A, Pace S and Huebener R P 2009 *Phys. Rev.* B **80** 144521
[13] Kunchur M N 2002 *Phys. Rev. Lett.* **89** 137005
[14] Babić D, Bentner J, Sürgers C and Strunk C 2004 *Phys. Rev.* B **69** 092510
[15] Vodolazov D Y and Peeters F M 2007 *Phys. Rev.* B **76** 014521
[16] Cuppens J, Ataklti G W, Moshchalkov V V, Silhanek A V, Van de Vondel J, de Souza Silva C C, da Silva R M and Albino Aguiar J 2011 *Phys. Rev.* B **84** 184507
[17] Lin N S, Heitmann T W, Yu K, Plourde B L T and Misko V R 2011 *Phys. Rev.* B **84** 144511
[18] Yu K, Hesselberth M B S, Kes P H and Plourde B L T 2010 *Phys. Rev.* B **81** 184503
[19] Reichhardt C J O and Reichhardt C 2010 *Phys. Rev.* B **81** 224516
[20] Soroka O K, Shklovskij V A and Huth M 2007 *Phys. Rev.* B **76** 014504
[21] Wördenweber R, Dymashevski P and Misko V R 2004 *Phys. Rev.* B **69** 184504
[22] Wördenweber R, Hollmann E, Schubert J, Kutzner R and Panaitov G 2012 *Phys. Rev.* B **85** 064503
[23] Jin B B, Zhu B Y, Wördenweber R, de Souza Silva C C, Wu P H and Moshchalkov V V 2010 *Phys. Rev.* B **81** 174505
[24] Palau A, Monton C, Rouco V, Obradors X and Puig T 2012 *Phys. Rev.* B **85** 012502
[25] Van de Vondel J, de Souza Silva C C, Zhu B Y, Morelle M and Moshchalkov V V 2005 *Phys. Rev. Lett.* **94** 057003
[26] Villegas J E, Smith K D, Huang L, Zhu Y, Morales R and Schuller I K 2008 *Phys. Rev.* B **77** 134510
[27] Perez de Lara D, Alija A, Gonzalez E M, Velez M, Martin J I and Vicent J L 2010 *Phys. Rev.* B **82** 174503
[28] Jaque D, Gonzalez E M, Martin J I, Anguita J V and Vicent J L 2002 *Appl. Phys. Lett.* **81** 2851–4
[29] Yuzhelevski Y and Jung G 1999 *Physica* C **314** 163–71
[30] González M P, Hollmann E and Wördenweber R 2007 *J. Appl. Phys.* **102** 063904

[31] Velez M, Martin J I, Villegas J E, Hoffmann A, Gonzalez E M, Vicent J L and Schuller I K 2008 *J. Magn. Magn. Mater.* **320** 2547–62
[32] Shklovskij V A and Dobrovolskiy O V 2006 *Phys. Rev.* B **74** 104511
[33] Shklovskij V A and Dobrovolskiy O V 2008 *Phys. Rev.* B **78** 104526
[34] Shklovskij V A and Dobrovolskiy O V 2011 *Phys. Rev.* B **84** 054515
[35] Huth M, Ritley K, Oster J, Dosch H and Adrian H 2002 *Adv. Funct. Mater.* **12** 333–8
[36] Utke I, Hoffmann P and Melngailis J 2008 *J. Vac. Sci. Technol.* B **26** 1197
[37] Dobrovolskiy O, Sachser R, Huth M and Shklovskij V A 2010 Even magnetoresistive response in thin nb films with washboard pinning nanostructures *Book of Abstracts of 4th Int. Congr. on Adv. Electromagnet. Mat. in Microwaves and Optics 'Metamaterials'* pp 528–30
[38] Dobrovolskiy O V, Huth M and Shklovskij V A 2010 *Supercond. Sci. Technol.* **23** 125014
[39] Dobrovolskiy O V, Begun E, Huth M, Shklovskij V A and Tsindlekht M I 2011 *Physica* C **471** 449–52
[40] Dobrovolskiy O V, Huth M and Shklovskij V A 2011 *J. Supercond. Nov. Magn.* **24** 375–80
[41] Dobrovolskiy O V, Huth M and Shklovskij V A 2013 to be published
[42] Shklovskij V A 2002 *Phys. Rev.* B **65** 092508
[43] Shklovskij V A and Sosedkin V V 2009 *Phys. Rev.* B **80** 214526
[44] Dobrovolskiy O V and Huth M 2012 *Thin Solid Films* **520** 5985–90
[45] Porrati F, Sachser R and Huth M 2009 *Nanotechnol.* **20** 195301
[46] Ziegler J F, Biersack J B and Littmarck U 1985 *The Stopping and Ranges of Ions in Solid* (New York: Pergamon)
[47] Wildes A R, Mayer J and Theis-Bróhl K 2001 *Thin Solid Films* **401** 7–34
[48] James A M and Lord M P 1992 *Macmillan's Chemical and Physical Data* (London: Macmillan)
[49] Grüneisen E 1926 *Handbuch der Physik* (Berlin: Springer) pp 1–59
[50] Bloch F 1930 *Z. Phys.* A **59** 208–14
[51] Ziman J M 1960 *Electrons and Phonons* (Oxford: Clarendon)
[52] Bid A, Bora A and Raychaudhuri A K 2006 *Phys. Rev.* B **74** 035426
[53] Gubin A I, Il'in K S, Vitusevich S A, Siegel M and Klein N 2005 *Phys. Rev.* B **72** 064503
[54] Chockalingam S P, Chand M, Jesudasan J, Tripathi V and Raychaudhuri P 2008 *Phys. Rev.* B **77** 214503
[55] Van Beelen H, Van Braam Houckgeest J, Thomas M H, Stolk C and De Bruyn Oubote R 1967 *Physica* **36** 241–53
[56] Wördenweber R, Sankarraj J, Dymashevski P and Hollmann E 2006 *Physica* C **434** 101–4
[57] Segal A, Karpovski M and Gerber A 2011 *Phys. Rev.* B **83** 094531
[58] Berlincourt T G 1959 *Phys. Rev.* **114** 969–77
[59] Beaulac T P, Pinski F J and Allen P B 1981 *Phys. Rev.* B **23** 3617–9
[60] Evtushinsky D V, Kordyuk A A, Zabolotnyy V B, Inosov D S, Büchner B, Berger H, Patthey L, Follath R and Borisenko S V 2008 *Phys. Rev. Lett.* **100** 236402
[61] Tinkham M 2004 *Introduction to Superconductivity* (New York: Mineola)
[62] Il'in K S, Rall D, Siegel M and Semenov A 2012 *Physica* C **479** 176–8
[63] Grimaldi G, Leo A, Zola D, Nigro A, Pace S, Laviano F and Mezzetti E 2010 *Phys. Rev.* B **82** 024512
[64] Kim D H, Kim K T, Hong H G, Hwang J S and Hahn T S 2003 *Cryogenics* **43** 561–5
[65] Pearl J 1964 *Appl. Phys. Lett.* **5** 65–6
[66] Maxfield B W and McLean W L 1965 *Phys. Rev.* **139** A1515–22
[67] Ando Y, Kubota H, Tanaka S, Aoyagi M, Akoh H and Takada S 1993 *Phys. Rev.* B **47** 5481–4
[68] Skocpol W J, Beasley M R and Tinkham M 1974 *J. Appl. Phys.* **45** 4054–66
[69] Likharev K K 1979 *Rev. Mod. Phys.* **51** 101–59
[70] Il'in K, Rall D, Siegel M, Engel A, Schilling A, Semenov A and Huebers H W 2010 *Physica* C **470** 953–6
[71] Shklovskij V A 1980 *J. Low Temp. Phys.* **41** 375–96
[72] Bezuglyj A and Shklovskij V 1992 *Physica* C **202** 234–42

[73] Flynn C P 1988 *J. Phys. F: Met. Phys.* **18** L195
[74] Delacour C, Ortega L, Faucher M, Crozes T, Fournier T, Pannetier B and Bouchiat V 2011 *Phys. Rev.* B **83** 144504
[75] Anderson P W 1962 *Phys. Rev. Lett.* **9** 309–11
[76] Palstra T T M, Batlogg B, Schneemeyer L F and Waszczak J V 1988 *Phys. Rev. Lett.* **61** 1662–5
[77] Besseling R, Kes P H, Dröse T and Vinokur V M 2005 *New J. Phys.* **7** 71